Tunable Magnetic Antiskyrmion Size and Helical Period from Nanometers to Micrometers in a D_{2d} Heusler Compound

Tianping Ma, Ankit K. Sharma, Rana Saha, Abhay K. Srivastava, Peter Werner, Praveen Vir, Vivek Kumar, Claudia Felser, and Stuart S. P. Parkin*

Skyrmions and antiskyrmions are magnetic nano-objects with distinct chiral, noncollinear spin textures that are found in various magnetic systems with crystal symmetries that give rise to specific Dzyaloshinskii–Moriya exchange vectors. These magnetic nano-objects are associated with closely related helical spin textures that can form in the same material. The skyrmion size and the period of the helix are generally considered as being determined, in large part, by the ratio of the magnitude of the Heisenberg to that of the Dzyaloshinskii–Moriya exchange interaction. In this work, it is shown by real-space magnetic imaging that the helix period λ and the size of the antiskyrmion d_{aSk} in the D_{2d} compound Mn$_{1.4}$PtSn can be systematically tuned by more than an order of magnitude from ≈100 nm to more than 1.1 µm by varying the thickness of the lamella in which they are observed. The chiral spin texture is verified to be preserved even up to micrometer-thick layers. This extreme size tunability is shown to arise from long-range magnetodipolar interactions, which typically play a much less important role for B20 skyrmions. This tunability in size makes antiskyrmions very attractive for technological applications.

One of the major topics in spintronics today is the study of the steady state and dynamical properties of spin textures with various topologies.[1] Amongst these are magnetic skyrmions (Sks) which are magnetic nano-objects with chiral magnetic boundaries, namely, an in-plane magnetized region that separates the interior and exterior of the object where the magnetization points up/down or vice versa. Another distinct magnetic nano-object, an antiskyrmion (aSks), that has a more complex

boundary than aSk, was recently discovered.[2] The boundaries in an aSk are composed of successive left-hand Bloch, left-hand Néel, right-hand Bloch, and right-hand Néel wall segments.[2] The intrinsic stability of aSks over a large range of field and temperature was recently demonstrated.[3] The detailed magnetic structures of both Sks and aSks are controlled by the magnitude and symmetry of the Dzyaloshinskii–Moriya exchange interaction (DMI).[4]

The dependence of Sks and helices on the thickness of the host material has been studied in several B20 materials including FeGe,[5] Mn$_{1-x}$Fe$_x$Ge of various compositions,[6] and Fe$_{0.5}$Co$_{0.5}$Si.[7] In all these cases no significant dependence of the size of the Sk or the helix period on the thickness of the host compound was found. It was concluded that the fundamental length scale is determined by a competition between the Heisenberg exchange and the DMI. By contrast, it was shown some time ago that the size and arrangement of achiral magnetic bubbles is strongly influenced by magnetostatic interactions.[8] What have been called "biskyrmions" and "skyrmions" in centrosymmetric materials fall into this latter category.[9] We show here that antiskyrmion systems are unique in that both DMI and magnetostatic interactions play a significant role and that, thereby, give rise to extensive size tunability as well as intrinsic stability. We demonstrate, using a combination of Lorentz transmission electron microscopy (LTEM) and magnetic force microscopy (MFM) that the size of the antiskyrmion scales with the period of the helical structure and that both can be tuned over a wide range of more than an order of magnitude by adjusting the thickness of the host layer in which they are imaged.

In these studies, we focus on exploring spin textures in thin lamellae formed from a single crystal of Mn$_{1.4}$PtSn which is an inverse tetragonal Heusler compound with D_{2d} symmetry (see Supporting Information). High-quality single crystals were prepared using a flux method. One single crystal was fashioned into a uniform thickness lamella (L1) and several wedge-shaped lamellae (L2–L4) by Ga$^+$ focused ion beam milling. The spin textures reported here were imaged using two different techniques. LTEM was used to both confirm the existence of aSks and to explore their size and the helix period for thinner wedges. Thicker wedges were studied using MFM. A schematic drawing of the aSk spin texture, that consists of chiral boundaries formed from helicoids (Bloch-like) and cycloidal

T. Ma, A. K. Sharma, Dr. R. Saha, A. K. Srivastava, Dr. P. Werner,
Prof. S. S. P. Parkin
Max Planck Institute of Microstructure Physics
Weinberg 2, Halle (Saale) D-06120, Germany
E-mail: stuart.parkin@mpi-halle.mpg.de
T. Ma, A. K. Sharma, A. K. Srivastava, Prof. S. S. P. Parkin
Institute of Physics
Martin Luther University
Halle-Wittenberg, Halle (Saale) D-06120, Germany
P. Vir, Dr. V. Kumar, Prof. C. Felser
Max Planck Institute for Chemical Physics of Solids
Nöthnitzer Straße 40, Dresden 01187, Germany

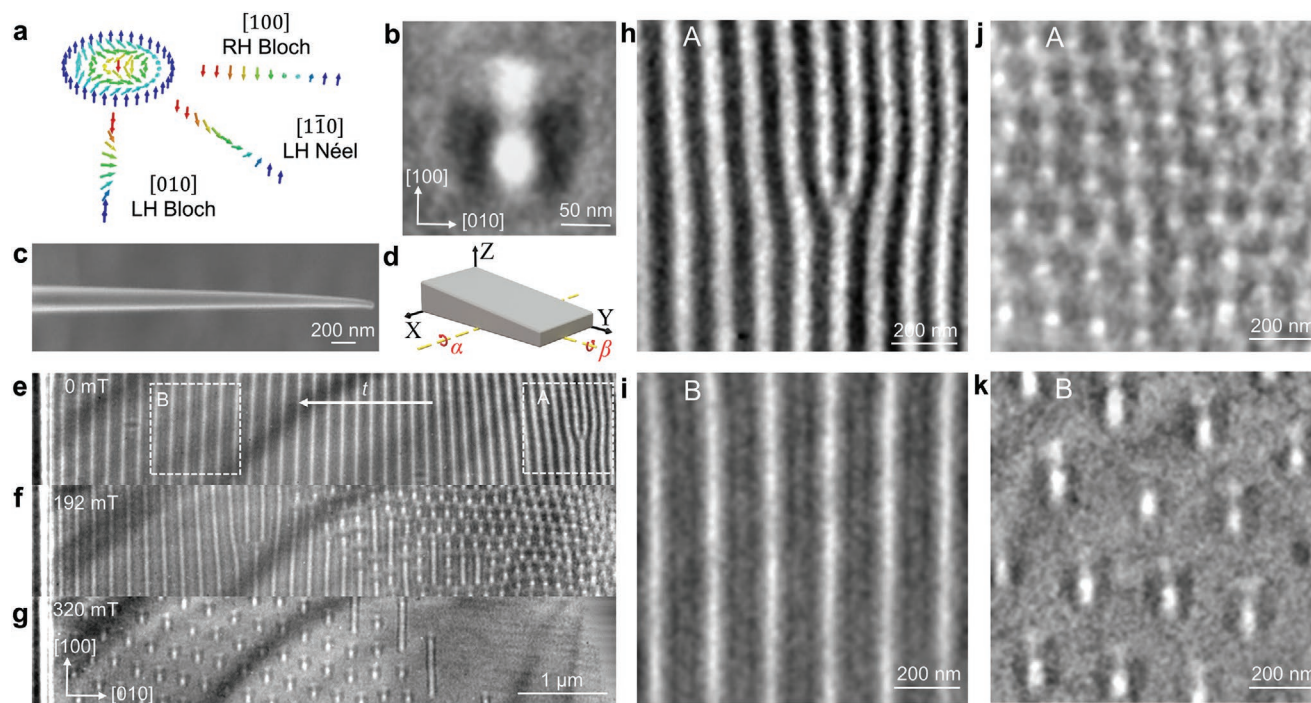The ORCID identification number(s) for the author(s) of this article can be found under https://doi.org/10.1002/adma.202002043.

Figure 1. LTEM images of chiral spin textures in $Mn_{1.4}PtSn$. a) Schematics of aSk and spin configurations along different crystallographic directions. b) LTEM image of a single aSk obtained from a uniform thickness lamella in the presence of a magnetic field of 368 mT. c) SEM image of a wedge-shaped lamella that is ≈6.4 µm long: the wedge is rotated by 35° so it looks foreshortened. d) Schematic of a lamella where α and β correspond to the double-stage tilt angles. e–g) LTEM images at 0, 192, and 320 mT. h,i) Helical magnetic phase in zero magnetic field and j,k) magnified images of the aSk phase in thinner and thicker regions of the wedge labeled A and B in (e). All LTEM images were recorded with an underfocus value of 1.5 mm except for (b) which was recorded at an underfocus value of 2 mm. The magnetic field is along [001] in all cases.

spin propagations (Néel-like), is shown in **Figure 1**a. Néel domain walls of right- and left-hand propagate along the [110] and [1$\bar{1}$0] directions, respectively, and Bloch domain walls of right- and left-hand propagate along the [100] and [010] directions, respectively. The helix in the D_{2d} system propagates along these latter directions (in the absence of an in-plane magnetic field) because its energy is lower for the Bloch structure (see Supporting Information).

Antiskyrmions were observed over a wide range of temperature and field in all samples. Only room temperature data are reported here because we find that the characteristic size of the spin textures in $Mn_{1.4}PtSn$ increases only a little as the temperature is reduced below room temperature, for otherwise the same thickness. Typical LTEM images are given in Figure 1 for a lamella with a uniform thickness of $t \approx 200$ nm (sample L1) and a wedged lamella whose thickness varies from ≈116 to ≈206 nm (sample L2). Figure 1b shows a magnified image of a single antiskyrmion in L1 that has a distinctive four-spot pattern with alternating black and white contrast, as previously observed for the closely related compound $Mn_{1.4}Pt_{0.9}Pd_{0.1}Sn$.[2] A scanning electron microscopy (SEM) image of the wedge L2 is shown in Figure 1c, and a schematic diagram showing the definition of the coordinate axes and tilting angles used in the discussion below is given in Figure 1d. Electron energy loss spectroscopy was used to determine the thickness t of the wedge.[10] The [001] zone axis is oriented along the transmission electron microscopy (TEM) column using a double-tilt sample holder. An LTEM image recorded in zero

magnetic field is shown in Figure 1e, in which the helices have been oriented along the [100] direction by using the in-plane component of an applied magnetic field. The most important finding is that the helix period varies significantly and monotonically from ≈96 to ≈185 nm as the sample thickness is varied from ≈116 to ≈206 nm. Magnified images of two representative regions A and B, each 1 µm × 1 µm in area, with thicknesses of ≈142 and ≈206 nm are shown in Figure 1h,i. The helix period is ≈108 ± 13 nm in region A (Figure 1h) and ≈185 ± 2 nm in region B (Figure 1i). Note that across the width of the wedge, where the thickness is unchanged, the helix period does not change significantly.

The helical state evolves into an aSk phase when a perpendicular magnetic field is introduced. A magnetic field oriented along the microscope column is generated by applying current in the objective lens of the TEM. The following protocol was used: after an LTEM image is taken, the sample's [001] axis is tilted away from the TEM column axis by $\alpha = 30°$ and the magnetic field is then increased in steps of 32 mT. Note that the presence of the in-plane field provided by the tilt allows for the aSk phase to be more easily stabilized.[2] The sample is then tilted back to 0° and the next LTEM image is recorded. This tilting procedure and step-wise increase in magnetic field is repeated until the magnetic field is so large that the sample reaches the fully magnetized ferromagnetic state. Typical LTEM images of L2 corresponding to fields of 192 and 320 mT are shown in Figure 1f,g. A complete sequence of LTEM images of the wedge, starting from a zero-field helical state with both [100] and [010] propagating

components, as the field is increased till the fully polarized state is reached, is shown in Figure S1 of the Supporting Information. These data illustrate the sensitivity of the field dependence of the spin texture to thickness. Moreover, it is clear that the size of the aSk, just like the helix period, depends strongly on the wedge thickness. This is more visible in Figure 1j,k that show magnified images of regions A (192 mT) and B (320 mT), in which the aSk size is respectively, $\approx 128 \pm 5$ and $\approx 200 \pm 4$ nm. As shown previously for $Mn_{1.4}Pt_{0.9}Pd_{0.1}Sn$,[2] the aSk size changes little with magnetic field. Thus, the aSk size variation arises predominantly from the change in thickness of the lamella rather than the change in magnetic field.

To explore possible variations in the aSk size and the helix period at thicknesses beyond those measurable by LTEM, we performed MFM measurements on two wedged lamellae with thicknesses varying from ≈ 630 to ≈ 4260 nm (L3) and ≈ 60 to ≈ 1600 nm (L4). The helical phase is clearly revealed in the MFM images. Typical results in zero magnetic field are summarized in **Figure 2**. An SEM image of the wedge L3 is shown in Figure 2a where the inset shows a schematic of the coordinate axis and the in-plane field direction φ_H. A saturation field of 1 T is applied in the plane of L3 at an angle φ_H and is then reduced to zero where the MFM image is taken: the MFM contrast corresponds to the stray field produced mainly by the out of plane magnetization component, M_z. By varying φ_H the helix propagation axis can be switched from predominantly [100] (Figure 2b, $\varphi_H = 180°$) to predominantly [010] (Figure 2c,

$\varphi_H = 90°$) or a mixture of both (Figure 2d, $\varphi_H = 135°$). A representative line profile of M_z taken from Figure 2c is show in Figure 2e. A typical 3D colormap of the helical region of an MFM image of wedge L4 is shown in Figure 2f. Both Figure 2e and Figure 2f clearly show a sinusoidal variation of M_z along the wedge, as well as a monotonic increase in helix period and amplitude with increasing lamella thickness. Note that the magnitude of the MFM signal increases approximately linearly with thickness. The helix period was determined from the peak to peak distance along an MFM line scan along the helix propagation direction, as shown in Figure 2e. The dependence of the helical period on the lamella thickness for all the wedges studied are shown in Figure 2g. Also included in the figure are LTEM data from Figure 1. The data show good agreement from wedge to wedge and between the LTEM and MFM techniques. The inset in Figure 2g shows the helical period variation for the wedge L2 obtained from LTEM studies and comparison with similar data on a wedge of comparable geometry for the sister compound $Mn_{1.4}Pt_{0.9}Pd_{0.1}Sn$.[2] The data closely resemble one another.

The helical phase transforms into an aSk phase in the presence of a magnetic field, as shown in **Figure 3** for wedge L3. Typical MFM images are shown for an initial field of zero, followed by magnetic fields of 300, 420, and 480 mT applied at 30° from the z-axis (Figure 3a–d) rotated toward the in-plane direction [010]. These images clearly show a gradual transformation from the helical phase into an aSk phase and finally into the
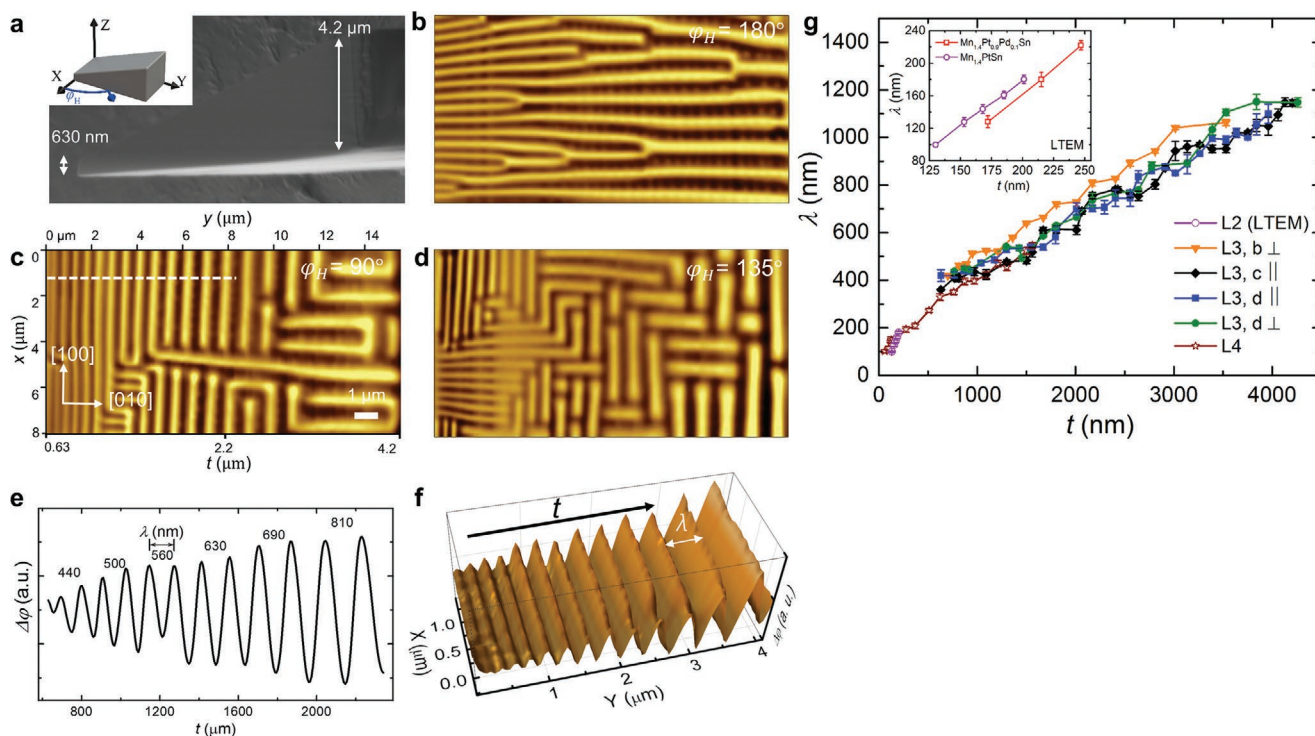

Figure 2. MFM images of helical spin textures in $Mn_{1.4}PtSn$. a) SEM image of the wedge-shaped lamella L3. The in-plane rotation angle φ_H is defined in the inset. b–d) MFM images with the helix aligned perpendicular (b), parallel (c), or both parallel and perpendicular (d) to the wedge. The size and thickness of the wedge are indicated in (c). The scanned area is 8×16 μm² where the lamella thickness increases from left to right. e) Line profile of MFM contrast, $\Delta\varphi$, along the white dashed line shown in (c). f) 3D colormap of $\Delta\varphi$ for wedge L4. g) Helix period as a function of thickness for wedges L3 and L4 for various orientations of the helices. Inset shows the variation of helical period with thickness in wedged lamellae of $Mn_{1.4}PtSn$ (L2) and $Mn_{1.4}Pt_{0.9}Pd_{0.1}Sn$ from LTEM studies. The error bar corresponds to the standard deviation of the helical period measured within the same thickness region.

2002043 (3 of 7)

**ADVANCED
SCIENCE NEWS**

www.advancedsciencenews.com
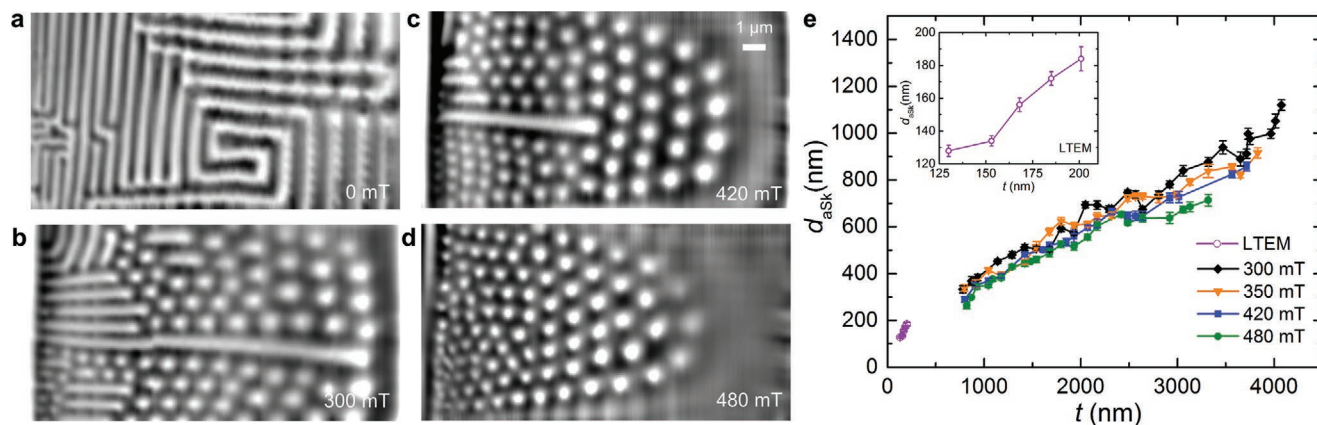
**ADVANCED
MATERIALS**

www.advmat.de

Figure 3. MFM images of antiskyrmion phase. a–d) Helical phase in zero magnetic field (a) and evolution to aSk phase as the field is increased to 300 mT (b), 420 mT (c), and 480 mT (d). The scanned area is 8×16 µm² where the thickness increases from left to right. e) aSk size versus thickness for various magnetic fields for wedge L4. Inset shows aSk size versus thickness for wedge L2 from LTEM images shown in Figure 1f,g.

fully polarized state that depends on sample thickness. The critical fields at which these transformations take place depend sensitively on the in-plane component of the field (see Supporting Information). A large thickness range where the aSks can be seen simultaneously was found for a tilt angle of $\approx 30°$ which also matches the tilt angle used for the LTEM data. At a field of ≈ 550 mT the complete wedge was fully magnetized.

The aSk phase could be stabilized at all thicknesses which enabled the dependence of the aSk size on the lamella thickness to be determined. These results are summarized in Figure 3e together with results from the LTEM data in Figure 1 that are shown in the inset to Figure 3e. The protocol used to determine the aSk size is discussed in the Supporting Information. The combined MFM and LTEM data clearly show that the aSk size has a weak dependence on magnetic field but a very strong dependence on the lamella thickness. Indeed, the aSk size increases by one order of magnitude from ≈ 128 nm to nearly 1.2 µm as the lamella thickness is varied from 142 nm to ≈ 4.2 µm. The aSk size and helix period are found to be close to one another for the same lamella thickness (see Figure S3, Supporting Information).

For the thinner wedge sample that is measured by LTEM, one can see from Figure 1 that the antiskyrmions appear at the thinner side first under a smaller field and then appear at the thicker side under a larger field. However, the result is opposite for the thicker wedge sample that is measured by MFM in Figure 3. These differences could arise from the different field tilting angles used in the measurements of these images, which is $\approx 0°$ for LTEM and $\approx 30°$ for MFM, or possibly from the different shapes (inclination angles) of the wedges used. However, the measured helix period and aSk size are hardly influenced by the measurement protocols or the wedge shapes.

In order to study the large-scale magnetic textures that we find in thicker lamellae, MFM measurements were performed in the presence of an in-plane magnetic field applied along distinct directions. We first apply an in-plane field of H = 1.5 T along the direction $\varphi_H = 0°$ to polarize the magnetization along +x, after which H is gradually decreased to 0.3 T. Then we observe that the magnetic texture has become triangularly shaped throughout much of the lamella (L3), as shown in **Figure 4**a. All the triangles point along the same direction: we

note that their size corresponds well to that of the original helix or aSk. Similar measurements for $\varphi_H = -90°$, $\varphi_H = -180°$, and $\varphi_H = -270°$ were performed, as shown in Figure 4b–d. In each case similar triangular magnetic textures are found but, most interestingly, they clearly point along different directions.

Let us consider the evolution of an aSk structure under an in-plane field applied along $\langle 100 \rangle$. Along these directions, the boundaries are Bloch like so that one expects that the area of the regions of in-plane magnetization within these boundaries pointing along the field direction will increase, whereas those pointing in the opposite direction will decrease in area. This will give rise to a distorted triangularly shaped object that is observed. Furthermore, when the field direction is rotated in a clockwise fashion, we find experimentally that the triangular shape rather rotates in the counterclockwise direction. This is in agreement with the expected distortion of the aSk structure under an in-plane magnetic field, as illustrated schematically in Figure 4e. Note that for a skyrmion structure, whether Bloch or Néel, the distorted spin textures would rotate in the same direction as the field. Another explanation for the triangularly shaped magnetic structures, which has recently been proposed, are "nontopological bubbles,"[11] in which half of the object is a square antiskyrmion and the other half is a round skyrmion. This "nontopological bubble" will also rotate in the opposite direction to the in-plane magnetic field. Since MFM cannot readily distinguish between an antiskyrmion and such a "nontopological bubble," the detailed magnetic structures, especially in the large thickness regime, require further studies. There is, however, strong experimental evidence, by comparing Figure 3 with Figure 4, that the round shape magnetic object in Figure 3 is indeed an antiskyrmion.

In order to probe the microscopic mechanism of the thickness dependence of the aSk size and helix period, an analytic calculation was carried out for a model D_{2d} system. The DMI energy density in a D_{2d} material is given by

$$E_{DMI} = D\left(m_x \frac{\partial m_z}{\partial y} + m_y \frac{\partial m_z}{\partial x} - m_z \frac{\partial m_x}{\partial y} - m_z \frac{\partial m_y}{\partial x} \right) \qquad (1)$$
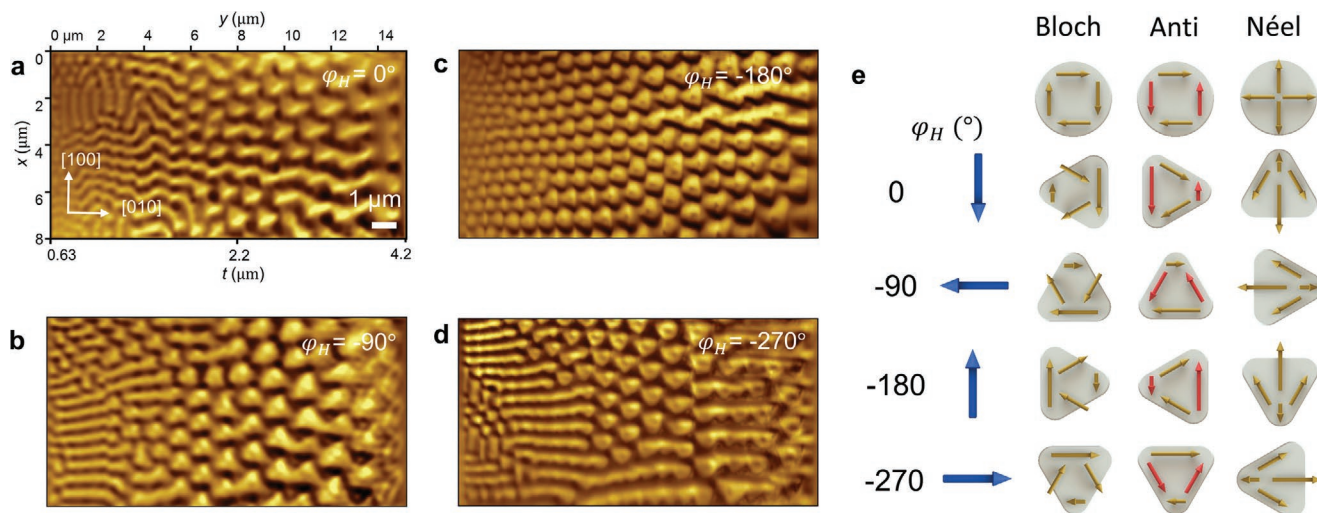
where D is the DMI strength (J m⁻²).

2002043 (4 of 7)

Figure 4. MFM images for different in-plane magnetic field directions. a–d) The field direction is $\varphi_H = 0°, -90°, -180°$, and $-270°$, respectively, and the field amplitude in each case is 0.3 T. e) Schematic spin textures for Bloch, antiskyrmion, and Néel skyrmion for different in-plane field directions. The blue arrow indicates the field direction. The red and yellow arrows indicate the in-plane magnetization. For the antiskyrmion, the arrows indicate the in-plane magnetization only for the Bloch regions of the boundary.

As shown in **Figure 5**a, we assume that the helix magnetization changes only along the helix direction with a Bloch sine function and a period of λ. The model assumes a slab of infinite extent in the xy plane and a finite thickness t along z. We assume the magnetization is constant along z which is a good approximation in a D_{2d} system where the DMI has no component along z. We note that this same assumption may not be appropriate for B20 systems in which the DMI imposes a twisted structure along z. The resultant total energy density is given by

$$E_{Tot} = E_{Exc} + E_{DMI} + E_{Ani} + E_{Dip}$$
$$= \frac{4\pi^2 A}{\lambda^2} - \frac{2\pi |D|}{\lambda} + \frac{K}{2} + \frac{\mu_0 M_s^2 \lambda}{8\pi t}\left(1 - e^{-\frac{2\pi t}{\lambda}}\right) \qquad (2)$$

where A is the exchange stiffness (J m^{-1}), K is the anisotropy energy (J m^{-3}), E_{Exc} is the volume exchange energy (J m^{-3}), E_{DMI} is the volume DMI energy, E_{Ani} is the volume magnetic anisotropy energy, E_{Dip} is the volume magnetic dipolar energy, and E_{Tot} is the volume total energy. Since the exchange interaction, DMI and anisotropy in this system are of bulk origin, there are no thickness dependent prefactors in the energy functionals. The DMI energy term does not depend on the helix/cycloid propagation direction.[12] The detailed calculations are summarized in the Supporting Information. Most importantly the long-range magnetostatic energy E_{Dip} can be given as an exact analytical expression. Atomistic numerical calculations were also carried out which agree well with this expression (see Supporting Information).

The dipolar energy as a function of helix period for various t are plotted in Figure 5b. When the film thickness is very small ($t \ll \lambda$), E_{Dip} can be simplified as $E_{Dip} = \frac{\mu_0 M_s^2}{4}\left(1 - \frac{\pi t}{\lambda}\right)$, so that E_{Dip} varies little in this thickness range. Similarly, when the film thickness is very large ($t \gg \lambda$), E_{Dip} is given by

$E_{Dip} = \frac{\mu_0 M_s^2 \lambda}{8\pi t}$, which has a linear dependence on λ with a very small slope. In these two regimes, the dipolar energy has a weak dependence on λ, as shown in Figure 5b for $t = 1$ nm and $t = 2500$ nm. However, for intermediate thicknesses (e.g., $t = 200$ nm), E_{Dip} changes significantly on the order of $\frac{\mu_0 M_s^2}{4}$ for the λ of interest.

The helix period corresponds to that which minimizes E_{Tot}. The calculated values of λ are summarized in Figure 5c,d for various ranges of model parameters. In Figure 5c the thickness and DMI strength dependent λ are shown as a colormap for constant A and M_s, whereas the thickness and M_s dependent λ are shown in Figure 5d for constant A and D. As shown in Figure 5c, when the DMI is very strong, λ is determined by $\frac{4\pi A}{|D|}$. When the DMI strength is weaker, λ drops rapidly to a minimum value as t is increased and then slowly increases back to $\frac{4\pi A}{|D|}$ for very thick layers. As shown in Figure 5d, when M_s is increased, λ shrinks.

The dipole energy is dominantly located at the surfaces of the lamella except for very thin t. As shown in Figures S10 and S11 of the Supporting Information, E_{Dip} is greatest at the surfaces, decaying exponentially into the interior of the lamella with a characteristic length-scale that is set by λ. Thus, in the limit of large t, the helix wavelength is no longer influenced by the dipole energy but is rather determined by the ratio of the Heisenberg and DMI energies. However, for the range of t of interest here the dipole energy strongly influences λ because, in very simplistic terms, the twisted helical structure reduces the dipole charge at the top and bottom surfaces. Since the total dipolar energy decreases, in this range, as $\approx 1/t$, thus λ monotonically increases as t is increased, thereby accounting for our experimental observation that λ approximately linearly increases with thickness. In Figure S13 of the Supporting Information a comparison between our experimental results and the model discussed above is made. Qualitatively the model
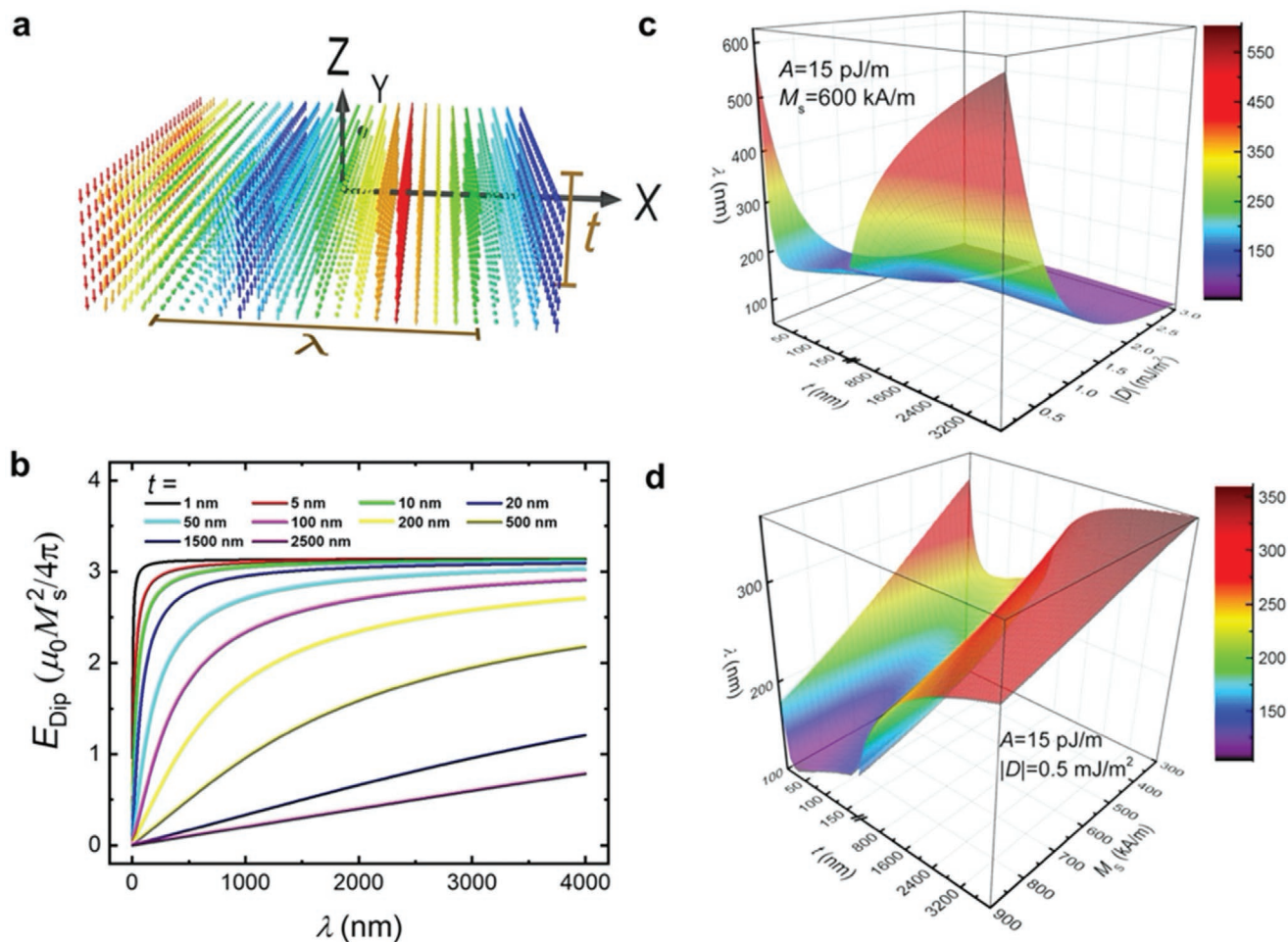
2002043 (5 of 7)

Figure 5. Model calculation for helix structure in D_{2d} system versus thickness. a) Schematic diagram of magnetic helical structure in a D_{2d} system with a helical period of λ and a thickness of t. b) Magnetodipolar energy per unit volume as a function of λ at various t. c) 3D colormap of λ versus t and DMI strength. d) 3D colormap of λ versus t and M_s.

accounts well for the observed trend of increasing λ with thickness. But it is difficult to find within the limitations of our model an exact agreement. We attribute this to deviations from the assumed pure helical Bloch-like form of the magnetic structure throughout the thickness. Our MFM data show that the helix structure is nearly sinusoidal and, since the magnitude of the MFM signal increases linearly with thickness, that the helix exists throughout the thickness. Nevertheless, there can clearly be deviations from this simple structure due to the complex interplay between all the relevant energy terms including the dipolar energy.

The calculation of the magnetodipolar interaction for the aSk phase is much more complicated and needs further theoretical studies. However, since, as shown in our experiments (Figures 2g and 3e), the helix period and aSk size are similar to each other, it is reasonable to assume that the same mechanism, i.e., the thickness dependence of the dipolar energy, accounts for the size variation of the aSk, as well as the helix period.

The thickness dependent behavior of the characteristic size of the spin texture reported in this work is distinct from other material systems due to important differences in the underlying

physical mechanisms. In magnetic bubble systems,[8] the magnetic structure is achiral since there is no DMI interaction. For a given thickness, the size of the bubble is not fixed and can vary strongly, and, moreover, has a significant dependence on the external magnetic field. Recently, our group reported the experimental discovery of Néel skyrmions in lamellae formed from PtMnGa which has a C_{3v} structure.[13] There, the Néel skyrmion size was also found to have a large thickness dependence. However, the width of the boundary of the Néel skyrmion is small compared to the size of the object itself, so that this system is more akin to conventional magnetic "bubbles." In an interfacial DMI system,[14] although it has been reported theoretically that dipolar interactions could play some role,[15] the effective strength of the DMI decreases with magnetic layer thickness, so limiting these systems to the nanometer thickness range.

In B20 bulk materials[5–7] the DMI has nonzero components along all three spatial directions, which is distinct from the D_{2d} system where the DMI is zero along the [001] direction. Thus, skyrmion tubes in a B20 material will have an additional twist in their magnetic structure along the tube direction. Such a twisted structure might weaken the contribution of the dipolar

interaction, thus resulting in a weak thickness dependence of the skyrmion size. Another type of twisted magnetic structure is a "Néel cap" in magnetic multilayer systems[16] or a horizontal Bloch line,[17] but these structures are induced by dipolar effects at the surface, and will be less influential than the twisted structures induced by DMI. Nevertheless, they may account for small differences between our experiments and model.

Thus, the D_{2d} antiskyrmion system is the only material system to date in which volume DMI and dipolar interactions together play an important role. This unique property ensures the stability of spin textures in this system over a very extended thickness range and their large size tunability. At the same time this competition between the D_{2d} volume DMI and dipolar interactions can lead to the formation of metastable elliptical Bloch skyrmions.[11,18]

In conclusion, our work shows how important is the role of the magnetodipolar interaction in influencing the size scale of noncollinear spin textures, depending on the symmetry of the host material. The wide range of tunability of the size of the antiskyrmion and corresponding helical spin textures in the D_{2d} system makes these materials particularly interesting for applications. For example, in racetrack memory devices[19] the size of antiskyrmions could be locally adjusted to make them easier to read and to create by adjusting the thickness of the racetrack spatially. Our results also clearly show how the size of antiskyrmions can be tuned by manipulating their magnetization rather than the DMI. For example, by chemical doping, by using materials with a strong temperature dependence of magnetization, or by the use of ferrimagnets or synthetic antiferromagnets, thereby opening up a new direction in the field of chiraltronics.

Supporting Information

Supporting Information is available from the Wiley Online Library or from the author.

Acknowledgements

Conflict of Interest

The authors declare no conflict of interest.

Keywords

[1] a) S. Mühlbauer, B. Binz, F. Jonietz, C. Pfleiderer, A. Rosch, A. Neubauer, R. Georgii, P. Böni, *Science* **2009**, *323*, 915; b) U. K. Rößler, A. N. Bogdanov, C. Pfleiderer, *Nature* **2006**, *442*, 797; c) X. Z. Yu, Y. Onose, N. Kanazawa, J. H. Park, J. H. Han, Y. Matsui, N. Nagaosa, Y. Tokura, *Nature* **2010**, *465*, 901; d) A. Fert, V. Cros, J. Sampaio, *Nat. Nanotechnol.* **2013**, *8*, 152; e) N. Nagaosa, Y. Tokura, *Nat. Nanotechnol.* **2013**, *8*, 899; f) W. Koshibae, N. Nagaosa, *Nat. Commun.* **2016**, *7*, 10542; g) F. Jonietz, S. Mühlbauer, C. Pfleiderer, A. Neubauer, W. Münzer, A. Bauer, T. Adams, R. Georgii, P. Böni, R. A. Duine, *Science* **2010**, *330*, 1648; h) A. Soumyanarayanan, M. Raju, A. G. Oyarce, A. K. Tan, M.-Y. Im, A. P. Petrović, P. Ho, K. Khoo, M. Tran, C. Gan, *Nat. Mater.* **2017**, *16*, 898; i) N. Romming, C. Hanneken, M. Menzel, J. E. Bickel, B. Wolter, K. von Bergmann, A. Kubetzka, R. Wiesendanger, *Science* **2013**, *341*, 636; j) A. N. Bogdanov, U. K. Rößler, M. Wolf, K.-H. Müller, *Phys. Rev. B* **2002**, *66*, 214410.
[2] A. K. Nayak, V. Kumar, T. Ma, P. Werner, E. Pippel, R. Sahoo, F. Damay, U. K. Rößler, C. Felser, S. S. P. Parkin, *Nature* **2017**, *548*, 561.
[3] R. Saha, A. K. Srivastava, T. Ma, J. Jena, P. Werner, V. Kumar, C. Felser, S. S. P. Parkin, *Nat. Commun.* **2019**, *10*, 5305.
[4] a) I. Dzyaloshinsky, *J. Phys. Chem. Solids* **1958**, *4*, 241; b) T. Moriya, *Phys. Rev.* **1960**, *120*, 91; c) A. N. Bogdanov, D. A. Yablonskii, *Zh. Eksp. Teor. Fiz.* **1989**, *95*, 182.
[5] a) X. Z. Yu, N. Kanazawa, Y. Onose, K. Kimoto, W. Z. Zhang, S. Ishiwata, Y. Matsui, Y. Tokura, *Nat. Mater.* **2011**, *10*, 106; b) F. Zheng, F. N. Rybakov, A. B. Borisov, D. Song, S. Wang, Z.-A. Li, H. Du, N. S. Kiselev, J. Caron, A. Kovács, *Nat. Nanotechnol.* **2018**, *13*, 451.
[6] K. Shibata, X. Z. Yu, T. Hara, D. Morikawa, N. Kanazawa, K. Kimoto, S. Ishiwata, Y. Matsui, Y. Tokura, *Nat. Nanotechnol.* **2013**, *8*, 723.
[7] H. S. Park, X. Yu, S. Aizawa, T. Tanigaki, T. Akashi, Y. Takahashi, T. Matsuda, N. Kanazawa, Y. Onose, D. Shindo, *Nat. Nanotechnol.* **2014**, *9*, 337.
[8] a) Z. Málek, V. Kamberský, *Czech. J. Phys.* **1958**, *8*, 416; b) J. Cape, G. Lehman, *J. Appl. Phys.* **1971**, *42*, 5732; c) P. Grundy, S. Herd, *Phys. Status Solidi A* **1973**, *20*, 295.
[9] a) X. Z. Yu, Y. Tokunaga, Y. Kaneko, W. Zhang, K. Kimoto, Y. Matsui, Y. Taguchi, Y. Tokura, *Nat. Commun.* **2014**, *5*, 3198; b) W. Wang, Y. Zhang, G. Xu, L. Peng, B. Ding, Y. Wang, Z. Hou, X. Zhang, X. Li, E. Liu, *Adv. Mater.* **2016**, *28*, 6887; c) X. Z. Yu, M. Mostovoy, Y. Tokunaga, W. Zhang, K. Kimoto, Y. Matsui, Y. Kaneko, N. Nagaosa, Y. Tokura, *Proc. Natl. Acad. Sci. USA* **2012**, *109*, 8856.
[10] T. Malis, S. Cheng, R. Egerton, *J. Electron Microsc. Tech.* **1988**, *8*, 193.
[11] L. Peng, R. Takagi, W. Koshibae, K. Shibata, K. Nakajima, T.-H. Arima, N. Nagaosa, S. Seki, X. Z. Yu, Y. Tokura, *Nat. Nanotechnol.* **2020**, *15*, 181.
[12] L. Camosi, N. Rougemaille, O. Fruchart, J. Vogel, S. Rohart, *Phys. Rev. B* **2018**, *97*, 134404.
[13] A. K. Srivastava, P. Devi, A. K. Sharma, T. Ma, H. Deniz, H. L. Meyerheim, C. Felser, S. S. P. Parkin, *Adv. Mater.* **2020**, *32*, 1904327.
[14] a) G. Chen, J. Zhu, A. Quesada, J. Li, A. N'Diaye, Y. Huo, T. Ma, Y. Chen, H. Kwon, C. Won, *Phys. Rev. Lett.* **2013**, *110*, 177204; b) G. Chen, T. Ma, A. T. N'Diaye, H. Kwon, C. Won, Y. Wu, A. K. Schmid, *Nat. Commun.* **2013**, *4*, 2671.
[15] a) I. Lemesh, F. Büttner, G. S. Beach, *Phys. Rev. B* **2017**, *95*, 174423; b) F. Büttner, I. Lemesh, G. S. Beach, *Sci. Rep.* **2018**, *8*, 4464.
[16] a) W. Legrand, N. Ronceray, N. Reyren, D. Maccariello, V. Cros, A. Fert, *Phys. Rev. Appl.* **2018**, *10*, 064042; b) I. Lemesh, G. S. Beach, *Phys. Rev. B* **2018**, *98*, 104402; c) S. Montoya, S. Couture, J. Chess, J. Lee, N. Kent, D. Henze, S. Sinha, M.-Y. Im, S. Kevan, P. Fischer, *Phys. Rev. B* **2017**, *95*, 024415.
[17] A. P. Malozemoff, J. C. Slonczewski, *Magnetic Domain Walls in Bubble Materials*, Academic Press, New York **1979**.
[18] J. Jena, B. Göbel, T. Ma, V. Kumar, R. Saha, I. Mertig, C. Felser, S. S. Parkin, *Nat. Commun.* **2020**, *11*, 1115.
[19] a) S. S. P. Parkin, M. Hayashi, L. Thomas, *Science* **2008**, *320*, 190; b) S. S. P. Parkin, S.-H. Yang, *Nat. Nanotechnol.* **2015**, *10*, 195.